



HAL
open science

SKPFM study of hydrogen in a two phase material. Experiments and modelling

E. Tohme, V. Barnier, F. Christien, C. Bosch, K. Wolski, M. Zamanzade

► To cite this version:

E. Tohme, V. Barnier, F. Christien, C. Bosch, K. Wolski, et al.. SKPFM study of hydrogen in a two phase material. Experiments and modelling. International Journal of Hydrogen Energy, 2019, 44 (33), pp.18597-18605. 10.1016/j.ijhydene.2019.05.177 . hal-02458249

HAL Id: hal-02458249

<https://hal.science/hal-02458249v1>

Submitted on 25 Oct 2021

HAL is a multi-disciplinary open access archive for the deposit and dissemination of scientific research documents, whether they are published or not. The documents may come from teaching and research institutions in France or abroad, or from public or private research centers.

L'archive ouverte pluridisciplinaire **HAL**, est destinée au dépôt et à la diffusion de documents scientifiques de niveau recherche, publiés ou non, émanant des établissements d'enseignement et de recherche français ou étrangers, des laboratoires publics ou privés.



Distributed under a Creative Commons Attribution - NonCommercial 4.0 International License

SKPFM study of hydrogen in a two phase material. Experiments and modelling.

E. Tohme, V. Barnier, F. Christien, C. Bosch, K. Wolski, M. Zamanzade

Mines Saint-Etienne, Univ Lyon, CNRS, UMR 5307 LGF, Centre SMS, F - 42023 Saint-Etienne France

Abstract

Scanning Kelvin Probe Force Microscopy (SKPFM) was used to study hydrogen diffusion in a duplex stainless steel. The experiments were conducted on specimens covered with a nanometric palladium layer and pre-charged with hydrogen. A finite element model (FEM) of hydrogen diffusion in a three phase system (ferrite, austenite and palladium) was developed to simulate the experiment. This model allows us to take into account the different diffusivity and solubility of hydrogen in the three phases. It is shown that the contrast observed in SKPFM correlates very well with the distribution of hydrogen in the palladium layer determined from FEM modelling. This contrast is governed mainly by the hydrogen release into the palladium layer. On the other hand there is no direct relation between the observed contrast and the hydrogen distribution in the stainless steel microstructure. Our results show that SKPFM should be considered as a way to monitor locally the release of hydrogen into the palladium layer, rather than a way to map the hydrogen concentration in the material.

Keywords

Scanning kelvin probe force microscopy; Hydrogen diffusion; FEM modelling, Duplex stainless steel.

1. Introduction

Hydrogen embrittlement of metals has been studied for several decades. Over the past century, techniques were developed in order to better understand the interactions between hydrogen and metal microstructure. Two of the most common techniques are the thermal desorption spectroscopy [1] and the gaseous or electrochemical permeation techniques [2]. These macroscopic techniques give us information about the impacts of microstructure on the mobility of hydrogen atoms and their trapping in lattice defects. However they should be ideally complemented by techniques allowing the localisation of the hydrogen in the microstructure. Direct analysis of hydrogen at the microstructure scale is exceptionally difficult although progress was made in the recent years using for example SIMS (secondary ions mass spectroscopy) [3] or APT (atom probe tomography) [4]. More recently, some studies proposed to use Kelvin probe microscopy (KPM) and AFM based scanning KPM (SKPFM) technique to detect hydrogen with high lateral resolution in various materials [5]. SKPFM can be used for local hydrogen detection, based on the variation of the electron work function with the changes in hydrogen content. Several studies have demonstrated some correlations between hydrogen behaviour and the measured potential using SKPFM in different materials, including mainly aluminium alloys [6] [7] and stainless steels [8] [9] [10] [11] [12]. In those studies, the observed space- and/or time-variations of the potential measured are discussed mainly in terms of local hydrogen concentration in the material. Some of those studies [6] [7] were conducted in air without any palladium layer covering the surface. The main disadvantage of this procedure is that the SKPFM measurement is actually conducted on an oxide layer, not on the metallic material itself. Any possible evolution of the oxide layer during the experiment is going to affect the measurement. This evolution of the oxide layer can be due to the oxygen present in the atmosphere and/or the desorbing hydrogen. In addition, the possible heterogeneities of the oxide layer related the material microstructure are usually not taken into account. Even when the experiments are conducted in nitrogen atmosphere [9] [10] [11] [12], it is impossible to avoid oxidation of the specimen surface, except for noble metals. To overcome this problem, the SKPFM measurements can be conducted on a material coated with a palladium thin layer which can prevent any variation in the state of the surface studied [13], [14]. In that configuration, the measurement is sensitive to the distribution of hydrogen in the palladium layer. It was

demonstrated by Evers et al. that the potential measured using SKPFM is related to the H^+ concentration in the nanoscopic water layer present at the surface of palladium at ambient atmosphere, which itself is in equilibrium with the local hydrogen content in the palladium [15]. So there is quite clear evidence in the literature that the potential measured in SKPFM is directly related to the hydrogen concentration in the palladium layer. However it can be questioned whether it does reflect the distribution of hydrogen in the material of interest located under the palladium layer. In this study, we tried to address this question by validating our experimental approach with a finite element model of hydrogen diffusion. The material used in this study is the duplex 2202 stainless steel. It was selected for several reasons. The two phases (ferrite and austenite) have very different hydrogen-related properties (diffusivity, solubility). It is then expected for the two phases to behave very differently with respect to hydrogen, thus enhancing possible H-related contrasts in SKPFM. In addition, the grain size is far above the lateral resolution of SKPFM, which facilitates the imaging procedure. Finally data are available (diffusivity [16] [17] and solubility [17] [18] of hydrogen at room temperature) for the two phases, which allows a reliable modelling of hydrogen diffusion in this system.

Previous works were conducted on the modelling of hydrogen diffusion in duplex stainless steels [19] [20] [21] [22]. However the usual Fick's equation was used in those works, which means that the difference of hydrogen solubilities in the two phases was just ignored. This is a drastic, and in most cases unrealistic, simplification. It is actually well known that the solubility of hydrogen is higher in austenite by orders of magnitude than in ferrite, so that, assuming an initial equal concentration in the two phases, there exists a driving force to transport hydrogen from ferrite to austenite. This phenomenon is known as "up-hill" diffusion after the works of Darken [23] on carbon in steels in 1949, in which diffusion is driven by the gradients of chemical potentials. The up-hill approach of solute diffusion is more general than the Fick approach where diffusion is assumed to be driven by concentration gradients. Very few studies addressed the diffusion of hydrogen in multiphase systems using the up-hill approach: this was done for solid-liquid aluminium alloys by Felberbaum et al. [24] and for duplex stainless steel by Olden et al. [17].

2. Material and experimental methods

The composition of the 2202 duplex stainless steel used in this study was determined by X-ray fluorescence and is shown in Table 1. Magnetic measurement using a sigmometer showed that the weight fraction of each phase is approximately 50%. The material was provided as a rolled plate 40 mm in thickness with pancake shaped grains parallel to the plate. A specimen $20 \times 20 \times 0.6 \text{ mm}^3$ was cut perpendicular to the rolling direction. A cross-section of that specimen is shown in Figure 1. The microstructure is characterized by very elongated islands of austenite (γ) embedded in a matrix of ferrite (α). The islands can sometimes cover the whole thickness of the specimen.

Both faces of the specimen were grinded and polished down to 1-micron diamond paste, and finished with silica suspension. One face of the sample (observation side) was then electrochemically etched using 60% sulfuric acid in order to reveal the topography, so that phases can be identified in the AFM as explained later. The etched face was then coated with 20 nm of palladium by physical vaporization deposition (PVD) using a PECS machine. The other face, i.e. the backside, was charged electrochemically with hydrogen for 24 hours at -1200 mV/SCE in deaerated water containing 30 g/L of NaCl. After electrochemical charging the sample was transported to the AFM chamber for SKPFM analysis. The time gap between H charging and SKPFM measurement was less than five minutes. It should be mentioned that H charging is carried out on one face only (backside) and that the specimen is not saturated in hydrogen at the end of charging.

The SKPFM measurements were conducted using a NanoWizard® 4 NanoScience AFM. The cantilever used is a MIKROMASCH conductive silicon tip, coated with platinum with a tip radius < 30 nm with a stiffness of 42 N/m and a resonance frequency of 350 kHz. The SKPFM

measurements were conducted in air using amplitude modulation detection and dual pass lift-up scan. The topography was measured in the first pass using intermittent contact mode. The contact potential difference (V_{CPD}) defined as:

$$V_{CPD} = \phi_{Tip} - \phi_{Sample} \quad (1)$$

with ϕ_{Tip} and ϕ_{Sample} the tip and sample work function respectively, was recorded in the second pass at a constant height of 50 nm above the sample. It should be mentioned that the contact potential difference may be defined differently in other papers, i.e. $V_{CPD} = \phi_{Sample} - \phi_{Tip}$. Both mechanical excitation for topography acquisition and electrical excitation for V_{CPD} measurement were made at the resonant frequency of the cantilever. ϕ_{Tip} is constant and hydrogen is known to decrease ϕ_{Sample} [14] [25]. Hence, higher V_{CPD} can be associated with higher hydrogen concentration in the palladium layer. In this paper the V_{CPD} will be referred to as "the potential".

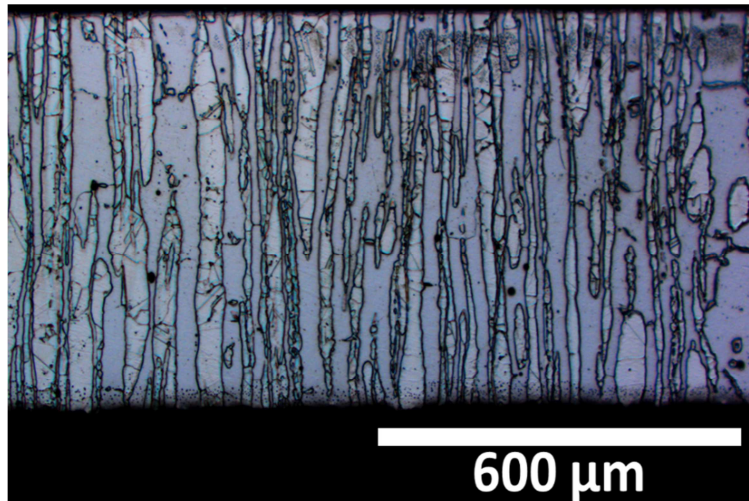


Figure 1 Microstructure observation on a cross-section of the duplex specimen used in this study. The image was obtained using optical microscopy after etching in 60% sulfuric acid.

Table 1 Composition of the duplex 2202 stainless steel used in this study (wt %).

Fe	Cr	Ni	Mn	Mo	Si
Bal.	23.16	2.64	1.29	0.23	0.41

Phase characterization was performed using EBSD. The measurements were carried out with a Carl Zeiss Σ IGMA series scanning electron microscope (SEM) equipped with an Oxford Instruments AZtec[®] EBSD system combined with Nordlys hardware. In order to correlate the SKPFM measurement of hydrogen with the microstructure of the duplex steel, a methodology is proposed here to identify the two phases α and γ directly from the topography measured using AFM.

Figure 2 shows a comparison between an EBSD phase map and an AFM topography image of a specific zone of the sample. It shows that sharp steps are present at the phase boundaries. Those steps are always ascending from ferrite to austenite. This is a result of the chemical etching conducted on the specimen. This particular feature allows us to identify the two phases unambiguously without the need of conducting an EBSD experiment on each analysed area.

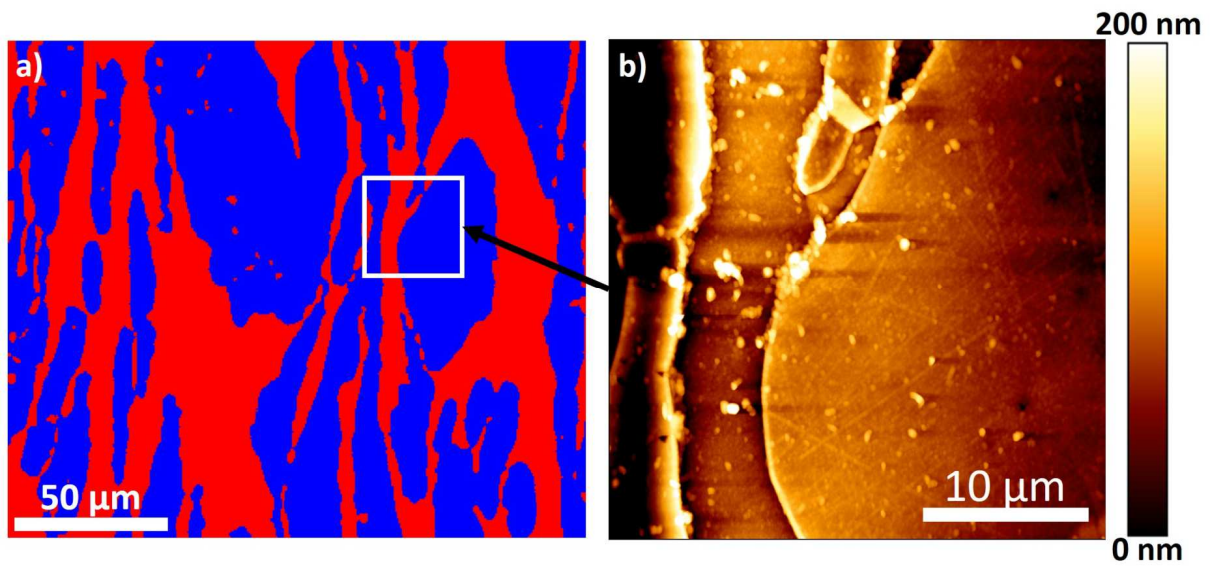


Figure 2: a) EBSD phase map with austenite in blue and ferrite in red, b) topography image measured by AFM of a specific zone (white square in EBSD phase map).

3. Modelling of hydrogen diffusion

A 2D finite element modelling of hydrogen diffusion across the specimen was conducted. The modelled specimen consists of a tri-phased system: duplex stainless steel (ferrite + austenite) and a palladium layer on the top (Figure 3). The simulated microstructure is representative of the actual one shown in Figure 1.

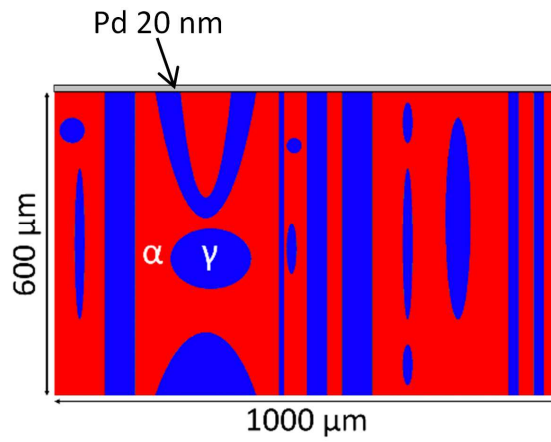


Figure 3 The geometry of the model used in the numerical study with austenite (γ) in blue, ferrite (α) in red and palladium layer in grey.

The different solubilities of hydrogen in the three phases were considered in the model. Instead of the usual Fick's law, the following equation (2) was used and implemented in COMSOL Multiphysics [17], [26]. This equation allows the modelling of up-hill diffusion of hydrogen from ferrite to austenite.

$$S \frac{\partial \left(\frac{C}{S} \right)}{\partial t} = \nabla \cdot \left(D S \nabla \left(\frac{C}{S} \right) \right) \quad (2)$$

where C is the hydrogen concentration in molar fraction, S is the hydrogen solubility in molar fraction, t is the time in seconds and D is the diffusion coefficient in $\text{m}^2 \cdot \text{s}^{-1}$. Eq. (2) is

obtained when considering that the hydrogen flux is governed by the hydrogen chemical potential gradient instead of the concentration gradient considered in the Fick's equation [26]. Eq. (2) is then more universal than the usual Fick's equation that in principle is not usable for a multiphase system.

For symmetry reasons, the left and right sides of the specimen in Figure 3 are isolated boundaries (i.e. no flux of hydrogen is allowed through those boundaries). A given fugacity f of hydrogen is imposed on the charging surface (bottom surface). This fugacity will give two different surface concentrations C_s of hydrogen in the two phases α and γ according to the Sievert law (Eq. (3)) [27].

$$C_s = S\sqrt{f} \quad (3)$$

The fugacity is set to a positive value (100 Bar) during the 24 hours of hydrogen charging, and then set to zero once the charging is finished. This means that for $t > 24$ h hydrogen desorption is allowed through the bottom surface. The boundary above the palladium layer is set as isolated. This means that no hydrogen desorption is allowed through that surface.

Table 2 shows the different parameters used in the finite element model. A hydrogen fugacity of 100 Bar was chosen here as a typical value corresponding to our conditions of cathodic charging [28]. The time of the simulation is chosen to cover the 24 hours of charging and the time of observation. The diffusion coefficients and the solubility of austenite and ferrite were taken from the literature (see references in Table 2).

The diffusion coefficient and the solubility of hydrogen in the palladium are not available in the literature for nanostructure Pd layers obtained from physical vapour deposition. It is assumed that the hydrogen is deeply trapped in the Pd layer due to the very high density of

crystal defects. This is why the solubility chosen is $S_{(Pd)} = 0.1 \text{ molar fraction} \cdot \text{Bar}^{-0.5}$. This value is chosen high enough to ensure that a driving force exists to transport hydrogen from the ferrite and the austenite into the palladium. It is higher than the solubility in bulk (Pd) [29], because of the trap sites. The hydrogen diffusion coefficient $D_{(Pd)}$ chosen here is $10^{-18} \text{ m}^2 \text{ s}^{-1}$, which is lower by orders of magnitude than the bulk diffusion coefficient [30]. There is evidence in the literature that diffusion of hydrogen in nano-grain palladium is indeed extremely slow. Using SKPFM in conditions similar to ours, Evers et al. [15] observed practically no lateral diffusion of hydrogen in a 100 nm Pd layer after 100 hours at room temperature. Assuming that they may have had anyway a lateral diffusion distance of $1 \mu\text{m}$ at maximum in 100 hours, this gives a diffusion coefficient of approximately $10^{-18} \text{ m}^2 \text{ s}^{-1}$ at maximum, which is the input value chosen in the model. The corresponding diffusion time across the 20 nm Pd layer is about 400 s, which is short compared to the observation time in SKPFM (some hours or tens of hours).

Table 2 Parameters used for the simulation of hydrogen diffusion in the duplex stainless steel using COMSOL.

Simulation time	10^6 seconds
Numbers of meshing elements	1462610
Number of boundary meshing elements	74550
Diffusion coefficient in ferrite	$D_{\alpha} = 6 \times 10^{-11} \text{ m}^2 \cdot \text{s}^{-1}$ [16] [17]
Diffusion coefficient in austenite	$D_{\gamma} = 1.4 \times 10^{-16} \text{ m}^2 \cdot \text{s}^{-1}$ [18] [17]
Diffusion coefficient in palladium	$D_{\text{Pd}} = 10^{-18} \text{ m}^2 \cdot \text{s}^{-1}$
Solubility in ferrite	$S_{\alpha} = 2.8 \times 10^{-8} \text{ molar fraction} \cdot \text{Bar}^{-0.5}$ [31], [32]
Solubility in austenite	$S_{\gamma} = 7 \times 10^{-5} \text{ molar fraction} \cdot \text{Bar}^{-0.5}$ [32], [33]
Solubility in palladium	$S_{\text{Pd}} = 0.1 \text{ molar fraction} \cdot \text{Bar}^{-0.5}$
Fixed fugacity of the charging medium	$f = 100 \text{ Bar}$

4. Results

4.1. Experimental results

Figure 4 shows one typical studied area of a specimen. Two types of ferrite grains are observed: “big” grains connected to other ferrite grains (those connected grains are marked “ α ” in Figure 4 b), and “small” grains embedded in bigger austenite grains (those embedded grains are marked “ α_e ” in Figure 4 b).

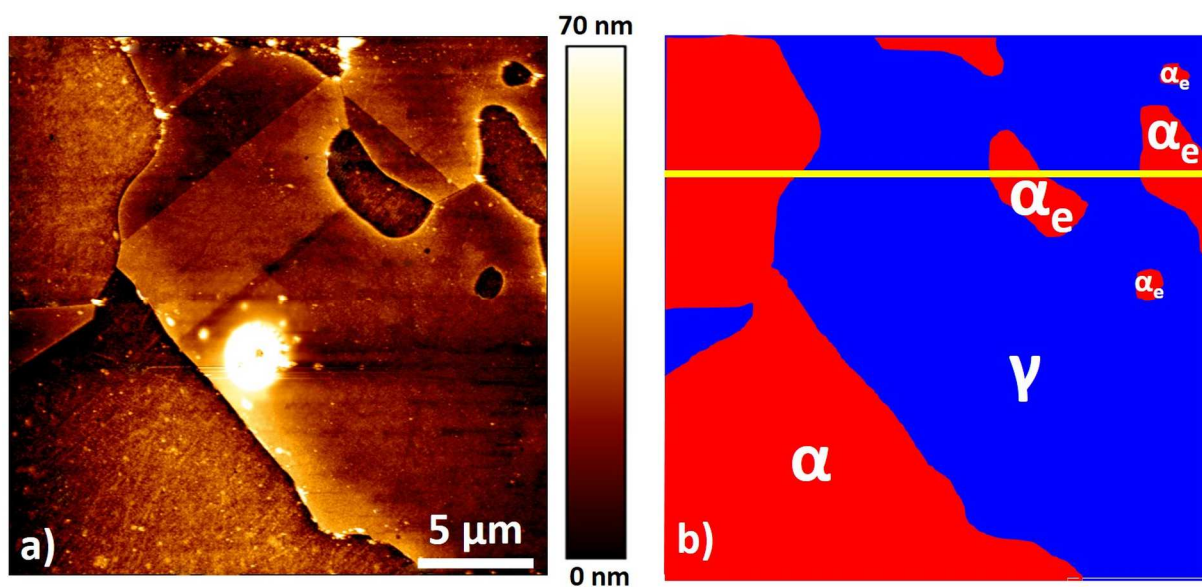


Figure 4 a) AFM topography map of the analysed region, b) identification of ferrite (α and α_e) and austenite (γ) phases

Figure 5 shows the time-dependency of the potential obtained on the specimen region shown in Figure 4. It is observed that the ferrite grains become brighter than the austenite grains. The contrast develops much slower (or does not develop at all) for the ferrite grains embedded in austenite (α_e) seen in the upper right part of the region. The contrast stabilizes after some hours and remains visible after several tens of hours of observation.

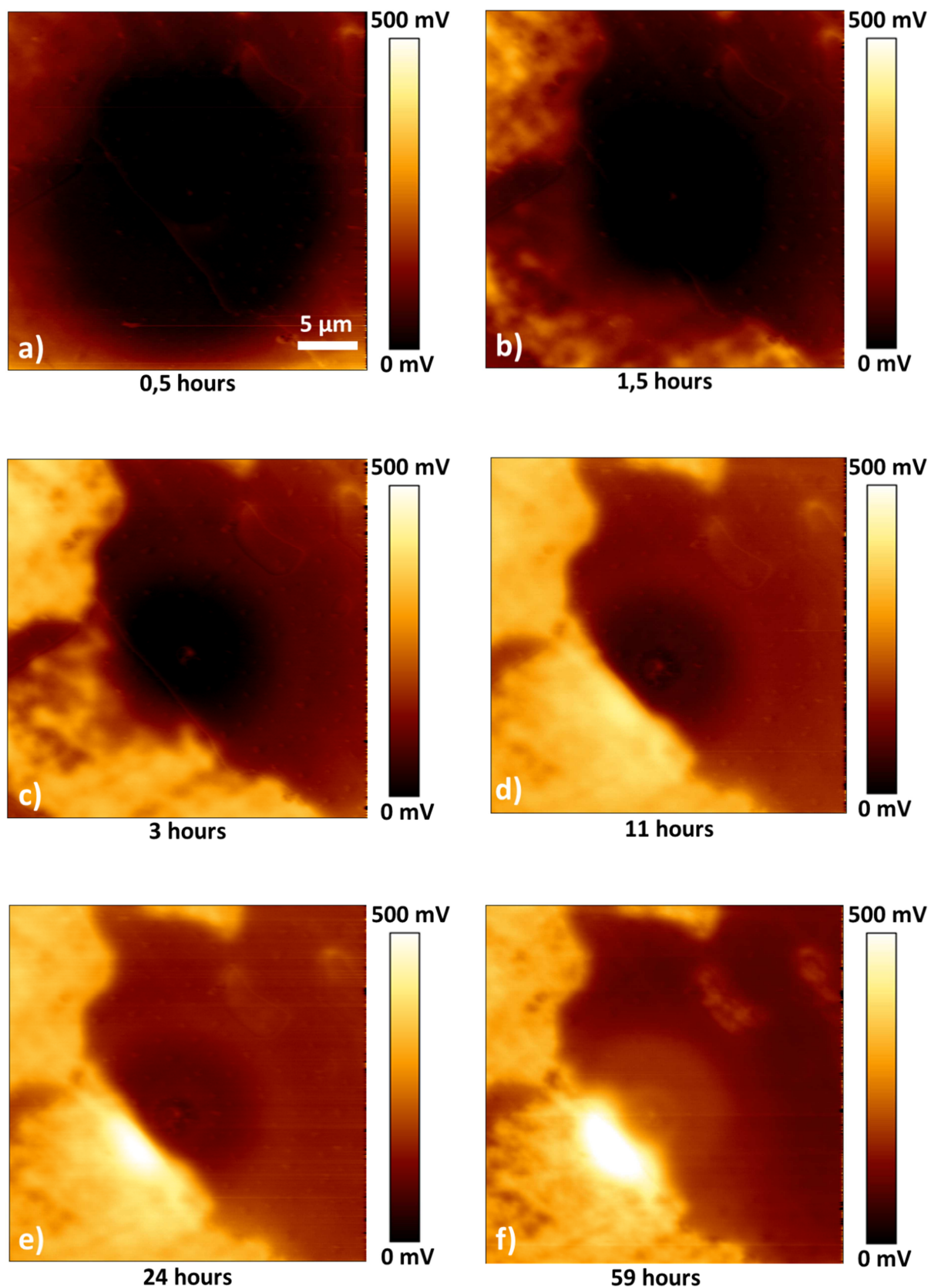


Figure 5 Ex-situ potential map measured by SKPFM at different times after electrochemical hydrogen charging. a) 0,5 hours, b) 1,5 hours, c) 3 hours, d) 11 hours, e) 24 hours and f) after 59 hours

Figure 6 shows more quantitatively the change of potential along the specific line shown in Figure 4 b). This confirms the observation previously described: the gap of potential between the ferrite and the austenite zones become deeper with time to the benefit of ferrite. However, for the two embedded ferrite grains (α_e) the potential increase with respect to the austenite is much slower and less pronounced than that observed for the big ferrite grains.

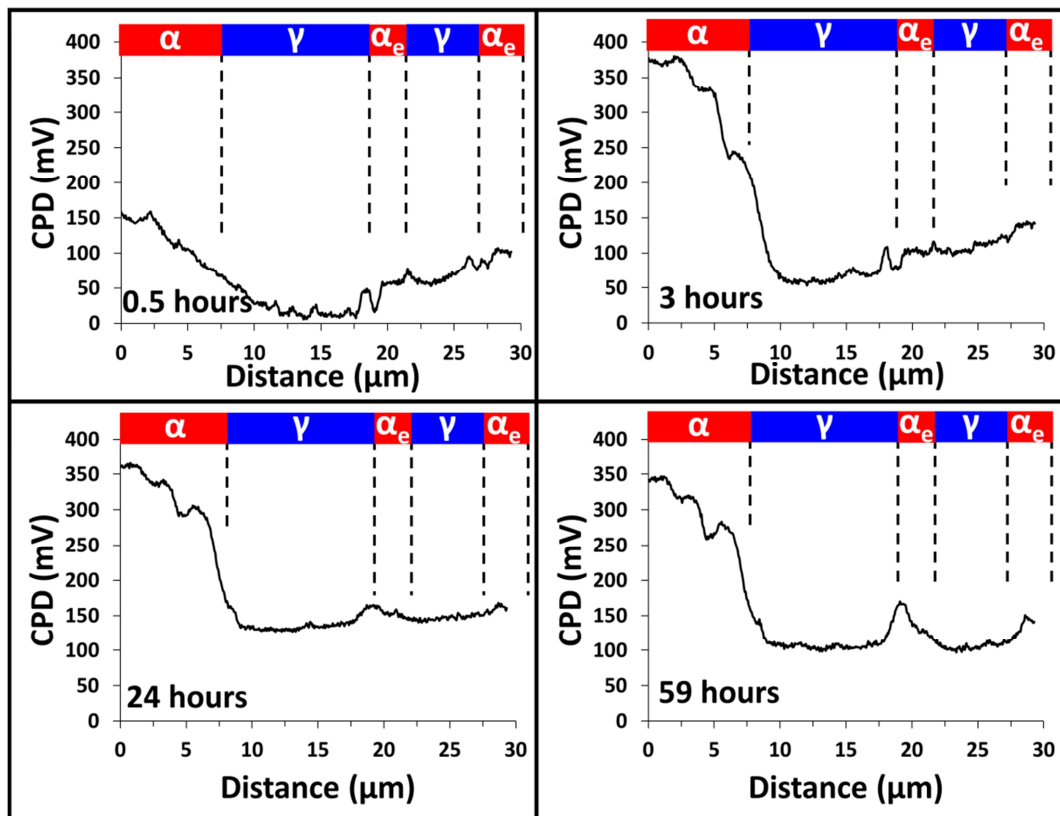


Figure 6 Potential line scan measured by SKPFM along the line indicated in Figure 4 b) at different times after hydrogen charging was stopped: 0.5 h, 3 h, 24 h and 59 h. Not too much attention is to be paid to the absolute values of potential. Only the potential variations between different places should be considered.

Because the potential increase is related to the hydrogen enrichment in the Pd film we can deduce that:

- First, the hydrogen enrichment is faster and more pronounced in the Pd above the ferrite grains. This is in agreement with the observations conducted by Evers et al. [15] with similar material and experimental conditions (hydrogen charging on the backside).
- Secondly, when analysing the ferrite grains (α_e) embedded in the austenite, this enrichment is almost inexistent, or at least very slow, and less pronounced.

This leads us to say that the hydrogen diffusion properties in the material influence significantly the entry of the hydrogen into the palladium layer. The high diffusivity in the ferrite would make the supply of hydrogen into the Pd film more efficient. On the other hand, the austenite has a low hydrogen diffusivity, which would make the hydrogen supply to the palladium layer less significant. These interpretations will be confirmed by finite element modelling.

4.2. Modelling of hydrogen diffusion

Figure 7 represents the hydrogen distribution in the cross-section of the specimen calculated from FEM modelling at different times. The hydrogen concentration is represented using a logarithmic colour scale.

The hydrogen concentration maps obtained are consistent with the solubility and diffusivity input data used for the two phases α and γ . First, the concentration tends to be much more homogeneous in the ferrite due to the high diffusivity of hydrogen in that phase.

Additionally, discontinuities of concentration are observed at interface boundaries. Those discontinuities are ascending from ferrite to austenite (up-hill diffusion) which is consistent with the hydrogen solubility in the two phases ($S_\gamma \gg S_\alpha$).

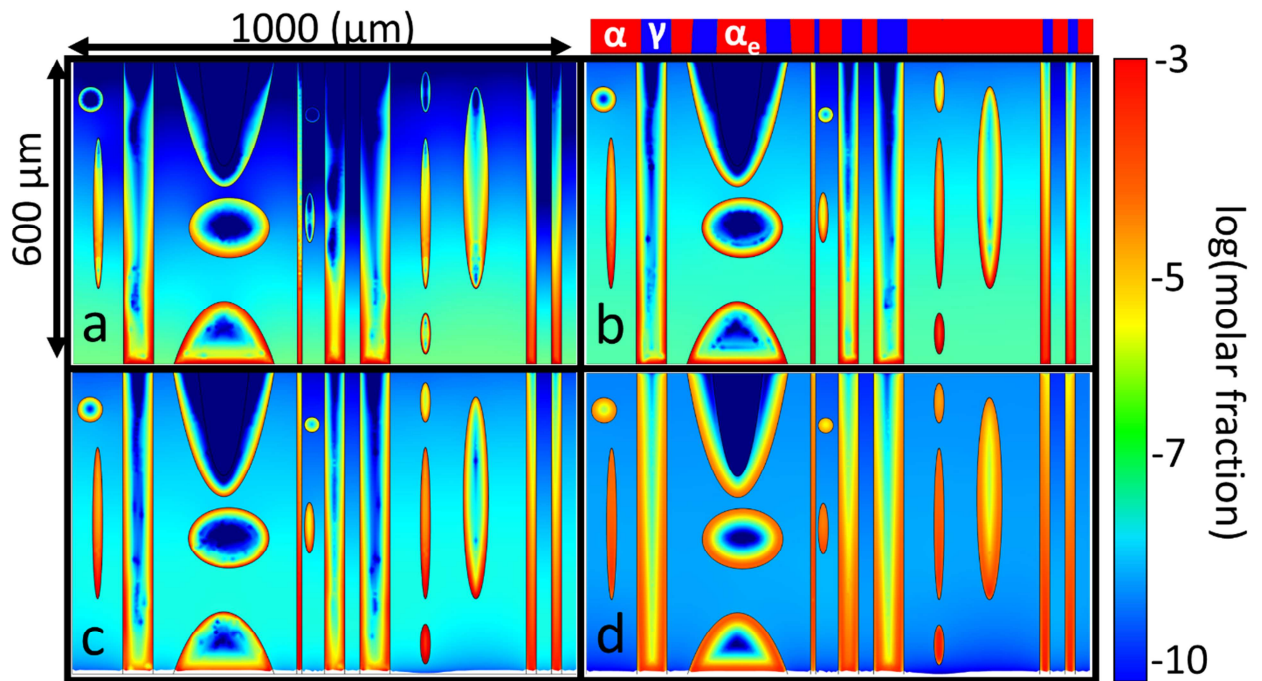


Figure 7 Cross-section hydrogen concentration maps calculated using FEM at different times: a) 2.4 hours of hydrogen charging, b) 24 hours (end) of charging, c) 24 h of charging + 3 hours of SKPFM observation and d) 24 h of charging + 59 hours of SKPFM observation. The Pd layer is not represented here. Note that hydrogen desorption occurs through the down side in c) and d).

Figure 8 represents the hydrogen distribution profile on the top of the palladium film at different time during charging and SKPFM observation. It is shown that over the time scale investigated here, the hydrogen concentration in the palladium layer increases significantly above ferrite while remaining close to zero above austenite. This is similar with what was

experimentally observed using SKPFM. This is strongly related to the fact that the hydrogen diffuses much faster in ferrite than in austenite. Even though the solubility of hydrogen in the ferrite is low, the ferrite can allow a fast transportation of hydrogen, which can explain the hydrogen enrichment of Pd film above the ferrite. The amount of hydrogen in the palladium film is related to the cumulative amount of hydrogen that is able to reach the palladium film through the two phases. Ferrite can provide more hydrogen than austenite to the palladium film.

Considering the ferrite grain α_e embedded in the austenite (grain centred in $x = 300 \mu\text{m}$ in Figure 7 and Figure 8), no hydrogen enrichment above this grain is observed. This can be explained by the fact that this grain is not percolated to the ferrite network. In other words, in order to reach this grain, the hydrogen must go through an austenitic zone, which in this case behaves as a barrier. These results are consistent with the experimental observations concerning the non-percolated ferrite grains (grains α_e in Figure 4, Figure 5 and Figure 6).

Figure 8 shows that the rate at which the hydrogen enrichment occurs in the palladium layer above different ferrite grains is variable from one to another (even excluding disconnected ferrite grains). It is likely due to the morphology of the ferrite grains: the large corridors of ferrite (see for example the one centred in $x=750 \mu\text{m}$ in Figure 8) provide more hydrogen to the palladium because it is less exposed to lateral “pumping” due to austenite grains than a narrow ferrite corridor (see for example in Figure 8 the ferrite regions centred in $x\approx 550 \mu\text{m}$ or $x\approx 940 \mu\text{m}$).

Figure 9 represents the hydrogen distribution profile in the steel ($2 \mu\text{m}$ under the palladium film) at different time during charging and SKPFM observation. Comparing Figure 8 with Figure 9, it is demonstrated that there is no obvious relation between the hydrogen

distribution in the Pd layer (which reflects the measurements done on SKPFM) and the hydrogen distribution in the steel under this layer. Figure 8 shows that the Pd layer enriches in hydrogen above the ferrite, while the concentration of hydrogen is higher in the austenite than in the ferrite. Figure 9 shows indeed that at $t = 24\text{h}$ (charging time) + 59h, the molar fraction of hydrogen can reach about $1.7 \cdot 10^{-5}$ in austenite (close to the interphase boundaries) while it is as low as $5 \cdot 10^{-9}$ in the ferrite. The absence of direct relation between the hydrogen distribution in the Pd layer and the hydrogen distribution in the steel microstructure suggests that the SKPFM technique (with a palladium layer) should not be considered as a direct method of local hydrogen mapping in the material. The technique is however sensitive to the local hydrogen release into the Pd layer.

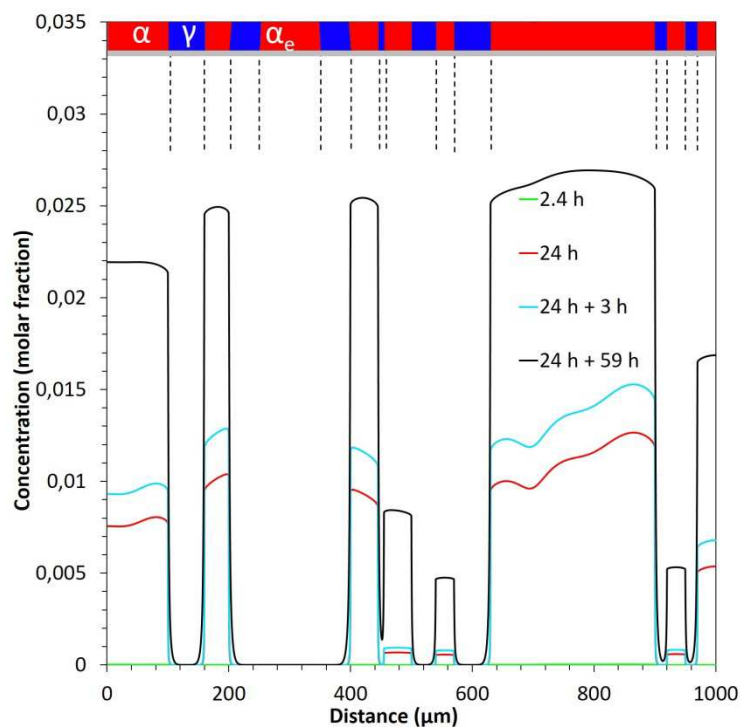


Figure 8 Hydrogen concentration profile at the surface of the palladium film at different time: 2.4 h of charging, and 24 hours (end) of charging, 24 h of charging + 3 and 59 hours of SKPFM observation. FEM modelling.

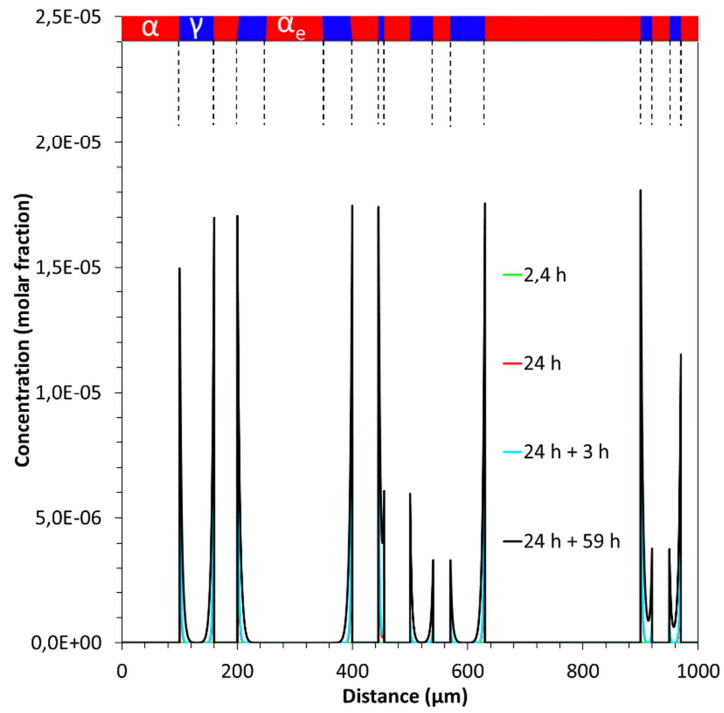


Figure 9 Hydrogen concentration profile in the steel (2 μm under the Pd film) at different time: 2.4 h of charging, and 24 hours (end) of charging, 24 h of charging + 3 and 59 hours of SKPFM observation. FEM modelling.

5. Conclusions

In this study, SKPFM was used for the detection of hydrogen in a duplex stainless steel. The SKPFM measurements were conducted in hydrogen pre-charged specimens coated with a thin layer of palladium. FEM modelling of the hydrogen diffusion during the experiment was conducted as well. The model developed takes account of the different hydrogen-related parameters (diffusion coefficient, solubility) in the three phases present (ferrite, austenite, palladium).

The main conclusions of this work can be summarized as follows:

- 1) Over the investigated timescale, only the ferrite phase can provide the palladium layer with a significant amount of hydrogen, thanks to the high hydrogen diffusion coefficient in ferrite compared to austenite. This explains why only the ferrite phase gets brighter in the SKPFM measurement.
- 2) It was observed that the embedded (non-percolated) ferrite grains provide much less hydrogen (or even no hydrogen at all in some cases) to the palladium layer. This is due to the surrounding shell of austenite that behaves as a hydrogen diffusion barrier in this case.
- 3) It was shown that the hydrogen concentration in the palladium layer (which gives the contrast obtained in SKPFM) does not reflect the hydrogen distribution in the underlying material. This is why the SKPFM method used in this study should be considered as a way to monitor locally the release of hydrogen into the Pd layer, rather than a way to map the local hydrogen distribution in the bulk material.

References

- [1] F. von Zeppelin, M. Haluška, and M. Hirscher, "Thermal desorption spectroscopy as a quantitative tool to determine the hydrogen content in solids," *Thermochim. Acta*, vol. 404, no. 1, pp. 251–258, Sep. 2003.
- [2] N. Boes and H. Züchner, "Electrochemical methods for studying diffusion, permeation and solubility of hydrogen in metals," *J. Common Met.*, vol. 49, pp. 223–240, Sep. 1976.
- [3] A. Oudriss *et al.*, "Meso-scale anisotropic hydrogen segregation near grain-boundaries in polycrystalline nickel characterized by EBSD/SIMS," *Mater. Lett.*, vol. 165, pp. 217–222, Feb. 2016.
- [4] Y.-S. Chen *et al.*, "Direct observation of individual hydrogen atoms at trapping sites in a ferritic steel," *Science*, vol. 355, no. 6330, pp. 1196–1199, Mar. 2017.
- [5] C. Senöz, S. Evers, M. Stratmann, and M. Rohwerder, "Scanning Kelvin Probe as a highly sensitive tool for detecting hydrogen permeation with high local resolution," *Electrochem. Commun.*, vol. 13, no. 12, pp. 1542–1545, Dec. 2011.
- [6] M. C. Lafouresse, M.-L. de Bonfils-Lahovary, C. Charvillat, L. Oger, L. Laffont, and C. Blanc, "A Kelvin probe force microscopy study of hydrogen insertion and desorption into 2024 aluminum alloy," *J. Alloys Compd.*, vol. 722, pp. 760–766, Oct. 2017.
- [7] C. Larignon, J. Alexis, E. Andrieu, L. Lacroix, G. Odemer, and C. Blanc, "Combined Kelvin probe force microscopy and secondary ion mass spectrometry for hydrogen detection in corroded 2024 aluminium alloy," *Electrochimica Acta*, vol. 110, pp. 484–490, Nov. 2013.
- [8] C. Örnek, P. Reccagni, U. Kivisäkk, E. Bettini, D. L. Engelberg, and J. Pan, "Hydrogen embrittlement of super duplex stainless steel – Towards understanding the effects of microstructure and strain," *Int. J. Hydrog. Energy*, vol. 43, no. 27, pp. 12543–12555, Jul. 2018.
- [9] B. An, Z. Hua, T. Iijima, C. Gu, J. Zheng, and C. San Marchi, "Scanning Kelvin Probe Force Microscopy Study of Hydrogen Distribution and Evolution in Duplex Stainless Steel," p. V06BT06A046, Jul. 2017.
- [10] Z. Hua, S. Zhu, J. Shang, G. Cheng, Y. Yao, and J. Zheng, "Scanning Kelvin probe force microscopy study on hydrogen distribution in austenitic stainless steel after martensitic transformation," *Mater. Lett.*, vol. 245, pp. 41–44, Jun. 2019.
- [11] Z. Hua, S. Zhu, B. An, T. Iijima, C. Gu, and J. Zheng, "The finding of hydrogen trapping at phase boundary in austenitic stainless steel by scanning Kelvin probe force microscopy," *Scr. Mater.*, vol. 162, pp. 219–222, Mar. 2019.
- [12] Z. Hua, B. An, T. Iijima, C. Gu, and J. Zheng, "The finding of crystallographic orientation dependence of hydrogen diffusion in austenitic stainless steel by scanning Kelvin probe force microscopy," *Scr. Mater.*, vol. 131, pp. 47–50, Apr. 2017.
- [13] S. Evers, C. Senöz, and M. Rohwerder, "Spatially resolved high sensitive measurement of hydrogen permeation by scanning Kelvin probe microscopy," *Electrochimica Acta*, vol. 110, pp. 534–538, Nov. 2013.
- [14] S. Evers and M. Rohwerder, "The hydrogen electrode in the 'dry': A Kelvin probe approach to measuring hydrogen in metals," *Electrochem. Commun.*, vol. 24, pp. 85–88, Oct. 2012.

-
- [15] S. Evers, C. Senöz, and M. Rohwerder, "Hydrogen detection in metals: a review and introduction of a Kelvin probe approach," *Sci. Technol. Adv. Mater.*, vol. 14, no. 1, p. 014201, 2013.
- [16] M. Skjellerudsveen, O. M. Akselsen, V. Olden, R. Johnsen, and A. Smirnova, "Effect of Microstructure and Temperature on Hydrogen Diffusion and Trapping in X70 grade Pipeline Steel and its Weldments," p. 13.
- [17] V. Olden, A. Saai, L. Jemblie, and R. Johnsen, "FE simulation of hydrogen diffusion in duplex stainless steel," *Int. J. Hydrog. Energy*, vol. 39, no. 2, pp. 1156–1163, Jan. 2014.
- [18] E. Owczarek and T. Zakroczymski, "Hydrogen transport in a duplex stainless steel," *Acta Mater.*, vol. 48, no. 12, pp. 3059–3070, Jul. 2000.
- [19] V. Olden, C. Thaulow, R. Johnsen, E. Østby, and T. Berstad, "Application of hydrogen influenced cohesive laws in the prediction of hydrogen induced stress cracking in 25%Cr duplex stainless steel," *Eng. Fract. Mech.*, vol. 75, no. 8, pp. 2333–2351, May 2008.
- [20] V. Olden, C. Thaulow, R. Johnsen, and E. Østby, "Cohesive zone modeling of hydrogen-induced stress cracking in 25% Cr duplex stainless steel," *Scr. Mater.*, vol. 57, no. 7, pp. 615–618, Oct. 2007.
- [21] T. Mente and T. Bollinghaus, "Modeling Of Hydrogen Distribution in A Duplex Stainless Steel," *Weld. World*, vol. 56, no. 11–12, pp. 66–78, Nov. 2012.
- [22] Yuhei S., Yoshiki M., and Masahito M., "Modeling of Hydrogen Diffusion Behavior Considering the Microstructure of Duplex Stainless Steel Weld Metal," *溶接学会論文集*, vol. 35, no. 2, pp. 23s–27s, 2017.
- [23] L. S. Darken, "Diffusion of carbon in austenite with a discontinuity in composition," *Trans AIME*, vol. 180, pp. 430–438, 1949.
- [24] M. Felberbaum, E. Landry-Désy, L. Weber, and M. Rappaz, "Effective hydrogen diffusion coefficient for solidifying aluminium alloys," *Acta Mater.*, vol. 59, no. 6, pp. 2302–2308, Apr. 2011.
- [25] R. F. Schaller and J. R. Scully, "Measurement of effective hydrogen diffusivity using the Scanning Kelvin Probe," *Electrochem. Commun.*, vol. 40, pp. 42–44, Mar. 2014.
- [26] J.-G. Sezgin, C. Bosch, A. Montouchet, G. Perrin, and K. Wolski, "Modelling and simulation of hydrogen redistribution in a heterogeneous alloy during the cooling down to 200 °C," *Int. J. Hydrog. Energy*, vol. 42, no. 30, pp. 19346–19358, Jul. 2017.
- [27] A. Sieverts, "Absorption of Gases by Metals," *Z. Für Met.*, vol. 21, pp. 37–46.
- [28] Q. Liu, A. D. Atrens, Z. Shi, K. Verbeken, and A. Atrens, "Determination of the hydrogen fugacity during electrolytic charging of steel," *Corros. Sci.*, vol. 87, pp. 239–258, Oct. 2014.
- [29] L. J. Gillespie and L. S. Galstaun, "The Palladium-Hydrogen Equilibrium and New Palladium Hydrides¹," *J. Am. Chem. Soc.*, vol. 58, no. 12, pp. 2565–2573, Dec. 1936.
- [30] G. L. Holleck, "Diffusion and solubility of hydrogen in palladium and palladium-silver alloys," *J. Phys. Chem.*, vol. 74, no. 3, pp. 503–511, Feb. 1970.
- [31] K. Kiuchi and R. B. McLellan, "The solubility and diffusivity of hydrogen in well-annealed and deformed iron," *Acta Metall.*, vol. 31, no. 7, pp. 961–984, Jul. 1983.
- [32] A. Turnbull and R. B. Hutchings, "Analysis of hydrogen atom transport in a two-phase alloy," *Mater. Sci. Eng. A*, vol. 177, no. 1, pp. 161–171, Apr. 1994.
- [33] P. Tsong-Pyng and C. J. Altstetter, "Effects of deformation on hydrogen permeation in austenitic stainless steels," *Acta Metall.*, vol. 34, no. 9, pp. 1771–1781, Sep. 1986.